ACS APPLIED MATERIALS

Research Article

# Revealing the Intrinsic Oxygen Evolution Reaction Activity of Perovskite Oxides across Conductivity Ranges Using Thin Film **Model Systems**

Lisa Heymann,\* Iris C. G. van den Bosch, Daan H. Wielens, Ole Kurbjeweit, Emma van der Minne, Ellen M. Kiens, Anton Kaus, Daniel Schön, Stephan Menzel, Bernard Boukamp, Felix Gunkel,\* and Christoph Baeumer\*



Cite This: ACS Appl. Mater. Interfaces 2025, 17, 21110-21121



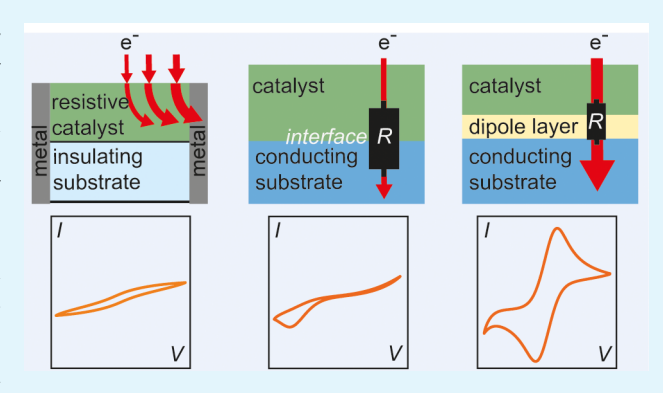
**ACCESS** 

Metrics & More

Article Recommendations

Supporting Information

ABSTRACT: The development of efficient electrocatalysts in water electrolysis is essential to decrease the high overpotentials, especially at the anode where the oxygen evolution reaction (OER) takes place. However, establishing catalyst design rules to find the optimal electrocatalysts is a substantial challenge. Complex oxides, which are often considered as suitable OER catalysts, can exhibit vastly different conductivity values, making it challenging to separate intrinsic catalytic activities from internal transport limitations. Here, we systematically decouple the limitations arising from electrical bulk resistivity, contact resistances to the catalyst support, and intrinsic OER catalytic properties using a systematic epitaxial thin film model catalyst approach. We investigate the influence of the resistivity of the three perovskite oxides LaNiO<sub>3- $\delta$ </sub> (3.7 × 10<sup>-4</sup>



 $\Omega$  cm),  $La_{0.67}Sr_{0.33}MnO_{3-\delta}$  (2.7 × 10<sup>-3</sup>  $\Omega$  cm), and  $La_{0.6}Ca_{0.4}FeO_{3-\delta}$  (0.57  $\Omega$ ·cm) on the observed catalytic activity. We tuned the electron pathway through the catalyst bulk by comparing insulating and conductive substrates. The conducting substrate reduces the electron pathway through the catalyst bulk from the millimeter to nanometer length scale. As we show, for the large electron pathways, the observed catalytic activity scales with resistivity because of a highly inhomogeneous lateral current density distribution. At the same time, even on the conducting substrate (Nb-doped SrTiO<sub>3</sub>), large contact resistances occur that limit the determination of intrinsic catalytic properties. By inserting interfacial dipole layers (in this case, LaAlO<sub>3</sub>) we lifted these interface resistances, allowing us to reveal the intrinsic catalytic properties of all examined catalysts. We find that  $La_{0.6}Ca_{0.4}FeO_{3-\delta}$  and  $LaNiO_{3-\delta}$  exhibit a similar intrinsic overpotential of 0.36 V at 0.1 mA/cm<sup>2</sup>, while their resistivities differ by 3 orders of magnitude. This finding shows that optimizing the electron pathway of the OER catalyst can lead the way to find new structure-activity relationships and to identify high-activity catalysts even if the electronic resistance is high.

KEYWORDS: electrocatalysis, oxygen evolution reaction, conductivity, resistivity, perovskite oxide, interface layer, intrinsic catalytic activity

#### INTRODUCTION

Electrochemical energy conversion technologies such as electrolyzers or fuel cells are crucial for renewable energy storage, e-fuel synthesis, and a non-fossil-based industry. 1,2 One prominent example is a water electrolyzer, where hydrogen is produced on the cathode via the hydrogen evolution reaction and oxygen is produced on the anode via the oxygen evolution reaction (OER). The optimization of catalytic processes taking place at the interface between catalyst and the electrolyte remain a challenge, particularly for the OER as it suffers from sluggish kinetics that limit the efficiency of the overall reaction.<sup>3,4</sup> Therefore, the catalytic properties of the OER catalyst must be optimized to decrease the OER overpotential.<sup>3,4</sup>

Perovskite oxides are one promising material class to reduce the high overpotentials in the OER. They exhibit an ABO<sub>3</sub> structure where the A-site is typically occupied by rare earth elements and alkaline earth elements and the B-site is occupied with transition metals. However, the electrical conductivity of perovskites varies by orders of magnitude, depending on the Bsite transition metal doping level and/or the defect structure of the material.<sup>6-8</sup> In the literature, it is often addressed that a

Received: November 29, 2024 Revised: February 11, 2025 Accepted: March 16, 2025 Published: March 31, 2025





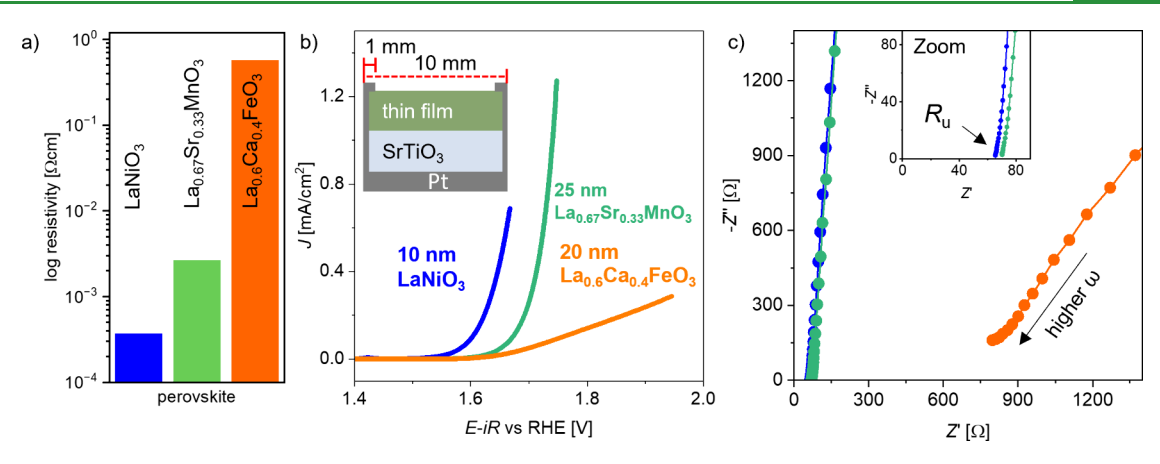


Figure 1. (a) Resistivity of LaNiO<sub>3-δ</sub>, La<sub>0.67</sub>Sr<sub>0.33</sub>MnO<sub>3-δ</sub> and La<sub>0.6</sub>Ca<sub>0.4</sub>FeO<sub>3-δ</sub>. (b) Cyclic voltammetry of LaNiO<sub>3-δ</sub>, La<sub>0.67</sub>Sr<sub>0.33</sub>MnO<sub>3-δ</sub> and La<sub>0.6</sub>Ca<sub>0.4</sub>FeO<sub>3-δ</sub> on SrTiO<sub>3</sub>, with Pt side contacts to the back. The film thickness of each material is given in the legend. The CV data are iR corrected and averaged between anodic and cathodic sweep from the second CV cycle (see also Figure S3). The sweep rate was 10 mV/s. (c) Nyquist plots in the high frequency ( $\omega$ ) range of LaNiO<sub>3-δ</sub>, La<sub>0.67</sub>Sr<sub>0.33</sub>MnO<sub>3-δ</sub>, and La<sub>0.6</sub>Ca<sub>0.4</sub>FeO<sub>3-δ</sub> measured at open circuit voltage (graph colors correspond to the legend in (b)). The inset shows a zoomed-in view of the Nyquist plot to the high frequency intercept of LaNiO<sub>3-δ</sub> and La<sub>0.67</sub>Sr<sub>0.33</sub>MnO<sub>3-δ</sub>.

high electrical conductivity, ensuring an unhindered electron pathway through the material bulk, is a crucial necessity for a good electrocatalyst. Therefore, perovskites with high resistivity are often described to be poor electrocatalysts such as LaFeO<sub>3</sub>, LaCoO<sub>3</sub>, or LaMnO<sub>3</sub><sup>10,11</sup> and low-conductivity perovskites have been discarded from catalyst research in some cases due to the difficulty to run sufficiently high current. <sup>12</sup>

However, it is hard to disentangle whether low electrochemical activity stems from high bulk resistivity or poor intrinsic catalytic properties. <sup>13,14</sup> The intrinsic catalytic properties reflect the ability to lower the kinetic barriers for the electrochemical reaction at the electrolyte/catalyst interface independent of their resistivity and additional stack resistances. For example, substituting Ni into the solid-solution series of La<sub>0.7</sub>Sr<sub>0.3</sub>Fe<sub>1-x</sub>Ni<sub>x</sub>O<sub>3-δ</sub> induces a phase transition and increased oxygen vacancy content leading to an overall lower resistivity that correlates with the OER performance. 15 Furthermore, LaCoO<sub>3</sub> shows comparably low OER activity in experiment, but lowering its resistivity through compressive lattice strain and introducing conductive support layers increases the OER activity. 16,17 Additionally, contact resistances (induced, e.g., through space charge layers) at the interface to the substrate or support layer can dilute the determination of intrinsic catalytic properties. 18-22 These examples indicate a correlation between electrical and electrochemical properties, yet it remains often unclear if a varied electrical resistivity directly affects the intrinsic catalytic activity of the OER catalyst. Further, the relations between electron transport pathways, bulk, and interface resistances remain unclear, and pathway-dependent current density losses are not quantified.

In this paper, we systematically decouple the intrinsic catalytic properties from bulk resistivity for perovskite oxides, covering a resistivity range of 3 orders of magnitude. We employ an epitaxial thin film model system approach to tune the electron transport pathway through the catalyst bulk and thin film stack. Single crystalline epitaxial thin films of perovskite oxides principally give the opportunity to reveal intrinsic properties.<sup>23–25</sup> These model catalysts are free of catalyst binder and conductive carbon and exhibit smooth surface morphologies with single crystal facet orientation,

allowing to determine catalytic properties also free of grain boundary effects. <sup>23,25,26</sup>

Here, we choose the three perovskite oxides LaNiO<sub>3-δ</sub>,  $La_{0.67}Sr_{0.33}MnO_{3-\delta}$ , and  $La_{0.6}Ca_{0.4}FeO_{3-\delta}$  as epitaxial thin films in (001) orientation, exhibiting the resistivities of  $3.7 \times 10^{-4} \Omega$ . cm,  $2.7 \times 10^{-3} \ \Omega$ ·cm, and  $0.57 \ \Omega$ ·cm, respectively. Metallic LaNiO<sub>3-δ</sub> and La<sub>0.67</sub>Sr<sub>0.33</sub>MnO<sub>3-δ</sub> are well studied electrocatalysts, especially for the OER and ORR (oxygen reduction reaction), 5,27,28 while La<sub>0.6</sub>Ca<sub>0.4</sub>FeO<sub>3.8</sub> was previously considered as an insufficient OER catalyst. 29 When the thin films are deposited on insulating substrates, the electron transport pathway through the bulk is several millimeters long and the observed OER activity follows the trend of the resistivities of the three perovskite oxides. To quantify inhomogeneous current density distributions, we conduct a COMSOL study, where the highly resistive La<sub>0.6</sub>Ca<sub>0.4</sub>FeO<sub>3-δ</sub> shows tremendous current density variations along the catalyst/electrolyte interface. Switching to conducting Nb-doped SrTiO<sub>3</sub> substrates decreases the electron transport pathway to nanometer length scales. However, large contact resistances occur between the substrate and thin films as also reported elsewhere. 22,30 Decreasing the contact resistance via interface engineering finally allows us to reveal the intrinsic catalytic properties of the three perovskites. Surprisingly, the initially inactive and highly resistive La<sub>0.6</sub>Ca<sub>0.4</sub>FeO<sub>3-δ</sub> thin film shows similarly high intrinsic OER activity as the metallic LaNiO<sub>3-δ</sub>, and La<sub>0.67</sub>Sr<sub>0.33</sub>MnO<sub>3-δ</sub> shows the lowest intrinsic OER activity. The results show that the intrinsic catalytic activity of electrocatalysts across large conductivity ranges can be determined when an appropriate and individualized sample design is applied.

### RESULTS

Epitaxial thin films of 10–25 nm thickness of LaNiO<sub>3-δ</sub>, La<sub>0.67</sub>Sr<sub>0.33</sub>MnO<sub>3-δ</sub>, and La<sub>0.6</sub>Ca<sub>0.4</sub>FeO<sub>3-δ</sub> were grown by pulsed laser deposition (PLD) on single crystal (100) SrTiO<sub>3</sub> substrates. The growth was tracked by reflection high energy electron diffraction (RHEED), enabling us to control the desired thin film thickness on the single unit cell level. Figure S1 shows representative RHEED data, X-ray diffraction (XRD), and atomic force microscopy (AFM), confirming the

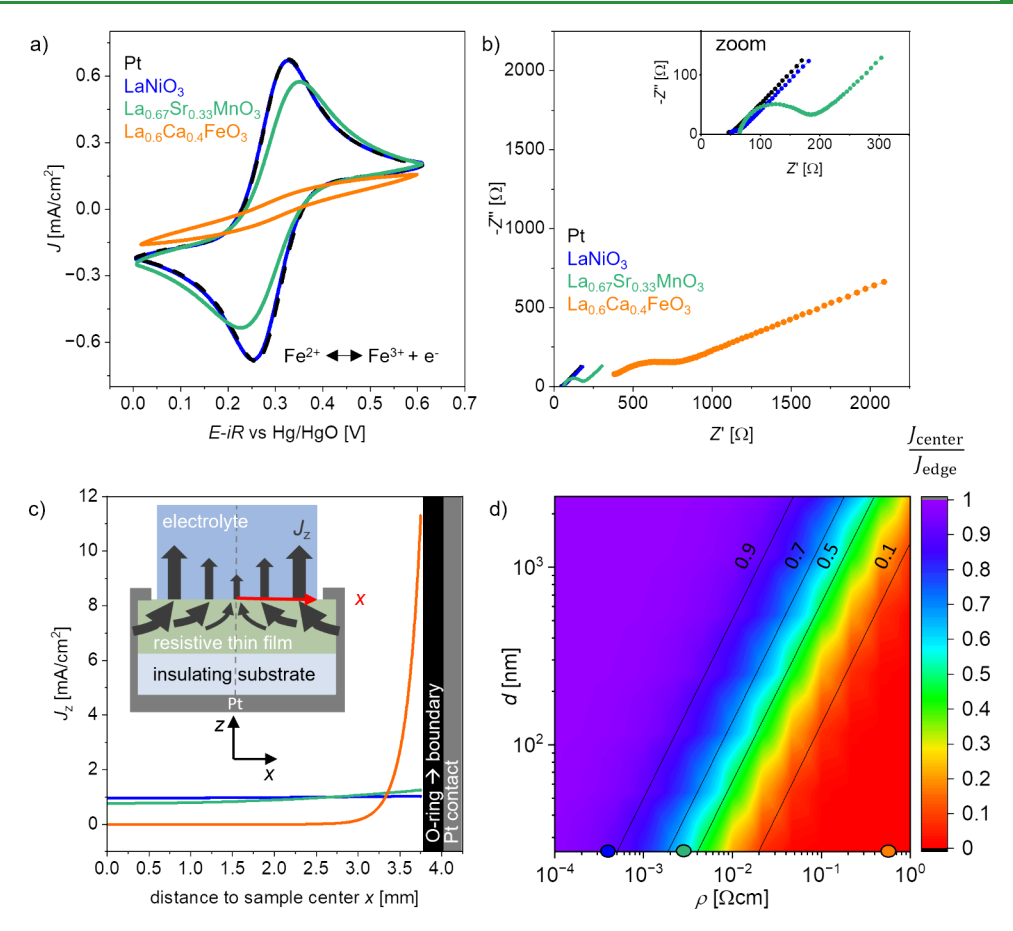


Figure 2. (a) CV scans of LaNiO<sub>3-δ</sub>, La<sub>0.67</sub>Sr<sub>0.33</sub>MnO<sub>3-δ</sub>, and La<sub>0.6</sub>Ca<sub>0.4</sub>FeO<sub>3-δ</sub> in K<sub>4</sub>[Fe(CN)<sub>6</sub>]/K<sub>3</sub>[Fe(CN)<sub>6</sub>] solution. The sweep rate was 30 mV/s.(b) Corresponding impedance spectroscopy measured at the OCP. The inset shows a zoom to the region of 350  $\Omega$  in the Z' direction. (c) Simulated current density distribution of the thin films on insulating substrates. The inset shows a sketch of the radial current density distribution  $J_z(x)$  on resistive thin films along the x-axis of the simulation. The dashed line in the center represents the axisymmetric line cut. (d) Heat map of the current density variation  $\frac{J_{center}}{J_{edge}}$  as a function of catalyst layer resistivity  $\rho$  and thickness d. Blue, green, and orange dots are the data points for 25 nm thick LaNiO<sub>3-δ</sub>, La<sub>0.67</sub>Sr<sub>0.33</sub>MnO<sub>3-δ</sub>, and La<sub>0.6</sub>Ca<sub>0.4</sub>FeO<sub>3-δ</sub> thin films, respectively.

well-defined synthesis of the OER model catalysts. The surface area determined by the AFM deviates by only 1.2% between samples, which has an insignificant impact on the catalytic activity. To determine the electrical resistivity  $(\rho)$ , the sheet resistance was measured in van der Pauw geometry. The resistivity of LaNiO $_{3-\delta}$  is  $3.7\times 10^{-4}~\Omega\cdot\text{cm}$  (Figure 1a) followed by  $\text{La}_{0.67}\text{Sr}_{0.33}\text{MnO}_{3-\delta}$  with 1 order of magnitude higher resistivity  $(2.7\times 10^{-3}~\Omega\cdot\text{cm})$  and finally  $\text{La}_{0.6}\text{Ca}_{0.4}\text{FeO}_{3-\delta}$  with 3 orders of magnitude higher resistivity  $(0.57~\Omega\cdot\text{cm})$ . The resistivity values of LaNiO $_{3-\delta}$  and La $_{0.67}\text{Sr}_{0.33}\text{MnO}_{3-\delta}$  grown on SrTiO $_3$  are consistent with the literature. To a sintered La $_{0.6}\text{Ca}_{0.4}\text{FeO}_{3-\delta}$  ceramic, a higher resistivity of 29  $\Omega$  cm was reported. The difference between the epitaxial thin film and sintered ceramic resistivity might stem from grain boundary effects or crystal facet dependent conductivity.

Electrochemical measurements were conducted in a three-electrode configuration with a rotating disc electrode (RDE). The thin film samples were mounted on the RDE shaft as illustrated in Figure S2a, using the same approach as reported previously.<sup>27</sup> For thin films deposited on insulating SrTiO<sub>3</sub> substrates, Pt was sputtered on the sample back side, edges, and front side edges (see sketch in Figure S2b and Figure 1b) to provide current collection from the sides of the thin film electrocatalysts.

The OER activity of LaNiO<sub>3-δ</sub>, La<sub>0.67</sub>Sr<sub>0.33</sub>MnO<sub>3-δ</sub>, and La<sub>0.6</sub>Ca<sub>0.4</sub>FeO<sub>3-δ</sub> was assessed using cyclic voltammetry (CV, Figure 1b). The CV scans were iR corrected with the uncompensated resistance (R<sub>u</sub>) obtained from open circuit potential (OCP) impedance spectroscopy (Figure 1c) with a linear extrapolation of the high frequency region to the x-axis. Note that the iR correction was applied to the CV curve after the electrochemical testing, as recommended<sup>25</sup> for a 100% iR correction. The displayed CV curves are the average of the forward and backward sweeps, as illustrated in Figure S3. The current density was determined for the geometric surface area, which is the area of the inner O-ring diameter. The LaNiO $_{3-\delta}$ thin film shows the highest OER activity with an overpotential  $(\eta = E_{OER} - 1.23 \text{ V})$  of 0.37 V at 0.1 mA/cm<sup>2</sup> followed by  $La_{0.67}Sr_{0.33}MnO_{3-\delta}$  with  $\eta = 0.44$  V. The  $La_{0.6}Ca_{0.4}FeO_{3-\delta}$  thin film shows the lowest OER activity with an overpotential of 0.53 V at 0.1 mA/cm<sup>2</sup>. The observed OER activity is hence scaling with the resistivity of LaNiO<sub>3-δ</sub>, La<sub>0.67</sub>Sr<sub>0.33</sub>MnO<sub>3-δ</sub> and  $La_{0.6}Ca_{0.4}FeO_{3-\delta}$ .

The CV scan of the  $La_{0.6}Ca_{0.4}FeO_{3-\delta}$  sample exhibits a close-to-linear slope at higher current densities, suggesting that an ohmic resistance suppresses the typically expected exponential behavior. This hints at a current limitation caused by the high bulk resistivity of  $La_{0.6}Ca_{0.4}FeO_{3-\delta}$ , rather than at a limitation caused by its intrinsic catalytic activity. The presence of an

additional ohmic resistance in addition to the electrolyte resistance is also apparent in the electrochemical impedance data (Figure 1c). The  $R_u$  values of LaNiO<sub>3 $\delta$ </sub> and  $La_{0.67}Sr_{0.33}MnO_{3-\delta}$  are 65  $\Omega$  and 70  $\Omega$  (cf. inset in Figure 1c), while the  $R_u$  of La<sub>0.6</sub>Ca<sub>0.4</sub>FeO<sub>3- $\delta$ </sub> is about an order of magnitude higher (724  $\Omega$ ). Further, the imaginary part of the impedance, -Z'', shows a larger offset from the abscissa. This occurs because the catalyst impedance signal overlaps with the impedance signal caused by the reference electrode (see Figure S4 for a detailed discussion). 22,35 Although the OER CV scan of La<sub>0.6</sub>Ca<sub>0.4</sub>FeO<sub>3- $\delta$ </sub> (Figure 1b) was iR corrected with the R<sub>u</sub> of 724  $\Omega$ , this *iR* correction appears to be insufficient to eliminate all ohmic resistances. A possible reason might be that the employed fitting procedure to determine  $R_{ij}$  underestimates the true serial resistances in the cell, e.g., due to the large offset from the abscissa. Alternatively, the x-axis offset as measured in impedance spectroscopy might not include all bulk related resistances, a point to which we will return below. Note that typical  $R_u$  values are between 40  $\Omega$  and 60  $\Omega$  in 0.1 M KOH with Pt electrodes in this cell geometry (see Figure S4a), indicating that our measured R<sub>u</sub> values contain a small contribution from sample-specific resistance (for LaNiO $_{3-\delta}$ and  $La_{0.67}Sr_{0.33}MnO_{3-\delta}$ ) or are dominated by sample resistance, as is the case for  $La_{0.6}Ca_{0.4}FeO_{3-\delta}$ .

The observed scaling with resistivity may be rationalized by the sample geometry. The chosen side-contacting implies that electrons released in redox reactions at the center of the  $10\times10~\text{mm}^2$  sample must travel up to 4 mm through the bulk of the catalyst layer to reach the metal contact (Figure S2b). The comparably high resistivity of La<sub>0.6</sub>Ca<sub>0.4</sub>FeO<sub>3-\delta</sub> suppresses the electron transport from the reaction site at the solid–liquid interface to the metallic contacts to a larger extent than is the case for LaNiO<sub>3-\delta</sub> and La<sub>0.67</sub>Sr<sub>0.33</sub>MnO<sub>3-\delta</sub>. Hence, the thin film resistivity might play a significant role in the measured OER activities.

To investigate this possible electron transport limitation in the thin film toward the metallic side contact independent of the sluggish OER kinetics, we employed CV in hexacyanoferrate  $K_4[Fe(CN)_6]/K_3[Fe(CN)_6]$  containing electrolyte, constituting the outer-sphere reversible redox couple hexacyanoferrate(II)/(III) (in the following denoted as hexacyanoferrate(II)/(III)). To obtain the typical duck shape of the CV scan, the rotation is turned off for this experiment. In contrast to inner-sphere electrocatalytic reactions like the OER, such outer-sphere fast redox couples have no significant material-dependent kinetic charge-transfer challenges but can directly reveal electronic transport limitations. For barrier-free band alignment at all involved interfaces and a low overall resistance, one expects a reversible redox process with symmetric anodic and cathodic peaks and a small peak potential separation. Any decrease in peak height as well as asymmetries can be related toward electronic resistances in the electrode stack<sup>24</sup> (or in some cases toward smaller surface areas<sup>36</sup>). The redox potential of hexacyanoferrate(II) to hexacyanoferrate(III) is 1.2 V vs RHE, which is similar to the theoretical OER redox potential, giving the advantage to test electron transport limitations in the relevant potential range.2

We compared the hexacyanoferrate(II)/(III) CV scans of 25 nm thick LaNiO<sub>3- $\delta$ </sub>, La<sub>0.67</sub>Sr<sub>0.33</sub>MnO<sub>3- $\delta$ </sub>, and La<sub>0.6</sub>Ca<sub>0.4</sub>FeO<sub>3- $\delta$ </sub> thin films to a Pt thin film acting as an ideally metallic reference (Figure 2a). LaNiO<sub>3- $\delta$ </sub> and Pt exhibit strongly overlapping CV curves, indicating that the electron transport

to the side contacts of the LaNiO $_{3-\delta}$  thin film is not limiting and the redox reaction exhibits no significant overpotential for LaNiO $_{3-\delta}$ . La $_{0.67}$ Sr $_{0.33}$ MnO $_{3-\delta}$  shows a slightly increased overpotential for the oxidation and reduction of hexacyanoferrate-(II)/(III), as indicated by the slight decrease and shift of the current density maximum toward higher and lower potentials, respectively. In contrast, La $_{0.6}$ Ca $_{0.4}$ FeO $_{3-\delta}$  exhibits no clear oxidation and reduction peaks in this potential range, indicating that its high resistivity strongly limits the electron transport.

As can be seen in Figure 2b, the corresponding impedance spectra recorded at the OCP in hexacyanoferrate(II)/(III) containing electrolyte show a similar behavior. LaNiO<sub>3- $\delta$ </sub> and Pt exhibit comparable spectra, whereas La<sub>0.67</sub>Sr<sub>0.33</sub>MnO<sub>3-δ</sub> exhibits a larger semicircle in the high frequency range. In the low frequency range, the impedance shows a nearly linear increase at an angle close to 45° for the Pt, LaNiO<sub>3-δ</sub>, and  $La_{0.67}Sr_{0.33}MnO_{3-\delta}$  thin films, indicating the presence of a semiinfinite Warburg element<sup>37</sup> in the equivalent circuit. This feature stems from the mass transport limitations of the hexacyanoferrate(II)/(III) species at the solid/liquid interface. The slight overpotentials observed for  $La_{0.67}Sr_{0.33}MnO_{3-\delta}$  in the CV scan in Figure 2a could stem from a higher resistivity compared to LaNiO<sub>3-δ</sub>, but the observed semicircle in the impedance indicates that there could be a significant interface barrier for the  $La_{0.67}Sr_{0.33}MnO_{3-\delta}$  thin film reducing the observed currents as well. For La<sub>0.6</sub>Ca<sub>0.4</sub>FeO<sub>3-δ</sub>, R<sub>u</sub> exhibits a significantly higher value since the higher total resistance of the thin film might add up to the overall observed x-axis offset, similar to the behavior of the impedance shown in Figure 1c. Moreover, the observed semicircle in the high frequency range is deformed, a characteristic often represented by a constant phase element in equivalent electrical circuits. The lowfrequency region shows a distorted incline with a slope of less than 45°, which indicates that the condition for an ideal Warburg element is not fulfilled either. Together, CV and impedance spectroscopy with the hexacyanoferrate(II)/(III) redox couple confirm that thin films with a high resistivity exhibit poor electrochemical performance due to impeded electron transport in the film.

To investigate and quantify the influence of the thin film resistivity on the local current density along the thin film/ electrolyte interface, a COMSOL Multiphysics study was conducted for the LaNiO<sub>3-δ</sub>, La<sub>0.67</sub>Sr<sub>0.33</sub>MnO<sub>3-δ</sub>, and La<sub>0.6</sub>Ca<sub>0.4</sub>FeO<sub>3-δ</sub> films, which is illustrated in Figure 2c. In the COMSOL simulation, a fixed current of 0.44 mA was applied, corresponding to an average current density of 1 mA/ cm<sup>2</sup> as the exposed geometric surface area is 0.44 cm<sup>2</sup>. We simulated the current density distribution  $J_z(x)$  across the catalyst surface from the sample center to the boundary of the catalyst, i.e., the location of the O-ring at 3.75 mm distance from the sample center. The metallic contacts are located in 4 mm distance to the sample center, approximating the real sample geometry in the RDE setup.  $J_z(x)$  is the current density perpendicular to the catalyst surface, with read-out along the sample interface in the x-direction (further details of the simulation can be found in the Methods section and in Figure S5). Our simulation focuses on the current distribution resulting from varying catalyst conductivity, assuming sufficient electrolyte conductivity to enable homogeneous current distribution for metallic electrodes. This is justified for the treatment of the OER, which is always characterized by slow electrode kinetics. These slow kinetics are imposed in the

simulation via an additional resistance at the electrode interface,<sup>38</sup> representing the OER charge transfer resistance.

The resulting current density distribution shows significant differences among the three materials with varying resistivities. For LaNiO<sub>3-8</sub>, the current density is almost homogeneously distributed, indicating that the low resistivity does not significantly affect the current pathway through the thin film toward the metallic contacts, and the entire catalyst area contributes similarly to the reaction current. In the sample center, the current density is 0.96 mA/cm<sup>2</sup> and increases to 1.04 mA/cm<sup>2</sup> at the catalyst boundary. To describe the current density variation along the sample profile, we define the ratio J<sub>center</sub>, which is the current density at the sample center in relation to the catalyst boundary:

$$\frac{J_{\text{center}}}{J_{\text{edge}}} = \frac{J_z(x = 0 \text{ mm})}{J_z(x = 3.75 \text{ mm})}$$

For LaNiO<sub>3- $\delta$ </sub>,  $\frac{J_{center}}{J_{edge}}$  is about 0.92. For La<sub>0.67</sub>Sr<sub>0.33</sub>MnO<sub>3- $\delta$ </sub>,

however, the current density in the sample center is only 0.76 mA/cm<sup>2</sup>, which is ~20% lower than the value obtained for LaNiO<sub>3-8</sub>. The current density increases continuously from the sample center toward the catalyst boundary reaching a current density of around 1.25 mA/cm<sup>2</sup>. Hence, the 1 order of magnitude higher resistivity in the  $La_{0.67}Sr_{0.33}MnO_{3-\delta}$  film leads to a significant change of the current density distribution along the interface, where  $\frac{J_{\text{center}}}{J_{\text{edge}}}$  is only 0.6. This behavior is even more

pronounced for La<sub>0.6</sub>Ca<sub>0.4</sub>FeO<sub>3-δ</sub>. Here, the current density is only 3.6 nA/cm<sup>2</sup> in the sample center and essentially does not contribute to the overall reaction. At a 3 mm radial distance, the current density increases to 0.15 mA/cm<sup>2</sup>. And only toward the edge, the current density increases drastically to more than 11 mA/cm<sup>2</sup> leading to an extremely small  $\frac{J_{center}}{J_{center}}$  ratio

of only  $2 \times 10^{-8}$ . Due to the high resistance of the La<sub>0.6</sub>Ca<sub>0.4</sub>FeO<sub>3-δ</sub> thin film, the area close to the metal contacts hence overproportionally contributes to the current and shows a locally higher current density (as sketched in the inset of Figure 2c). In the Supplementary Note N1, the possible inhomogeneities caused by electrolyte effects<sup>38</sup> are estimated for our setup, where the variation is only about 10% in the sample center. However, according to our COMSOL simulations, the inhomogeneities caused by the thin film catalyst resistivity can reach values that are orders of magnitude higher. Hence, inhomogeneities caused by electrolyte effects have a minor influence.

Hence, the COMSOL study shows that the effective surface area accessible for electrochemical reactions is extremely small for La<sub>0.6</sub>Ca<sub>0.4</sub>FeO<sub>3-δ</sub> in the chosen sample geometry. Therefore, for samples with higher resistivity, the observed electrochemical currents can effectively not be related to their geometric surface area that is exposed to the electrolyte, making it impossible to reveal their intrinsic catalytic properties in any electrochemical reaction in such sample geometry. The observed low activity of La<sub>0.6</sub>Ca<sub>0.4</sub>FeO<sub>3-δ</sub> (Figure 1b) thus results from ill-defined normalization of the current density with respect to the total exposed catalyst area.

To determine which resistivity-thickness relations are suitable to reveal the intrinsic properties for this sample geometry, we extended the COMSOL study for the full resistivity range from  $10^{-4}$  to  $1 \Omega$ ·cm and thin film thicknesses of up to 2.5  $\mu$ m. The expected current density ratio  $\frac{J_{center}}{J_{center}}$  is determined for various combinations of catalyst resistivity and layer thickness, yielding the heat map shown in Figure 2d. The values for 25 nm thick LaNiO<sub>3-δ</sub>, La<sub>0.67</sub>Sr<sub>0.33</sub>MnO<sub>3-δ</sub>, and La<sub>0.6</sub>Ca<sub>0.4</sub>FeO<sub>3-δ</sub> thin films are marked as blue, green, and orange dots, respectively.

We consider the LaNiO $_{3-\delta}$  case with  $\frac{J_{\rm center}}{J_{\rm edge}}=0.92$  as an acceptable scenario to extract intrinsic catalytic properties in this geometry, while for  $La_{0.67}Sr_{0.33}MnO_{3-\delta}$  with  $\frac{J_{center}}{J_{edge}}=0.6$  the current density would already be too inhomogeneous for a proper analysis. However, with an exemplary sample thickness of more than 200 nm,  $\frac{J_{\rm center}}{J_{\rm edge}}$  would be 0.9 or more also for  ${\rm La_{0.67}Sr_{0.33}MnO_{3-\delta t}}$  enabling us to principally reveal the intrinsic catalytic properties of  $La_{0.67}Sr_{0.33}MnO_{3\text{-}\delta}$  in this sample geometry. For La<sub>0.6</sub>Ca<sub>0.4</sub>FeO<sub>3-δ</sub>, however, even a film thickness of 1  $\mu$ m would only lead to  $\frac{J_{\text{center}}}{J_{\text{edge}}} = 0.2$ , making it impossible to determine the intrinsic catalytic properties in this sample geometry. Figure S6 shows the heat map on a logarithmic scale, highlighting the extremely small  $\frac{J_{\mathrm{center}}}{J_{\mathrm{edge}}}$  values for resistivities above  $2 \times 10^{-2} \ \Omega \cdot cm$ .

We emphasize that even though the trends presented in Figure 2d will be valid for any geometrical setup, i.e.,  $\frac{\int_{\text{center}}}{r}$ increases with increasing film thickness or decreasing film resistivity, the absolute values of  $\frac{J_{\text{center}}}{J_{\text{center}}}$  depend also on the lateral

geometry of the experimental setup. If the setup deviates greatly from that used here, additional simulations would be required to accurately estimate the variation in the current density across the interface between the thin film and the electrolyte. Nevertheless, the heat map can be used as qualitative guidance for any thin film geometry applied to the OER catalysis. We also note that ohmic drops in the solution can lead to an additional inhomogeneity. While the expected variation in current density across the electrode surface caused by electrolyte effects is much smaller than the effects observed for our highly resistive catalysts, it would be necessary to explicitly include the electrode kinetics model developed by Newman<sup>38</sup> in simulations for high-resistivity catalysts for mass-transfer limited reactions, where the electrolyte effects become more relevant.

The previously mentioned ill-defined normalization of the current density in La<sub>0.6</sub>Ca<sub>0.4</sub>FeO<sub>3-δ</sub> can also explain the deformed impedance features observed in Figure 2b. As the current-potential distribution exhibits a strong radial distribution, the equivalent electric circuit needs to be described as a series of  $R_u$ -RC elements that vary along the solid/liquid interface. Such 2D surface distributions are experimentally observed as a constant phase element in the global impedance, 39-41 thus explaining the suppressed impedance feature in the high and low frequency ranges observed for La<sub>0.6</sub>Ca<sub>0.4</sub>FeO<sub>3-δ</sub>. An additional reason for the non-ideal Warburg element in Figure 2b could be sideward diffusion of ionic species in the electrolyte, which has been observed as an edge effect<sup>42</sup> that can principally also occur on metallic electrodes. The phenomenon of varied radial current-

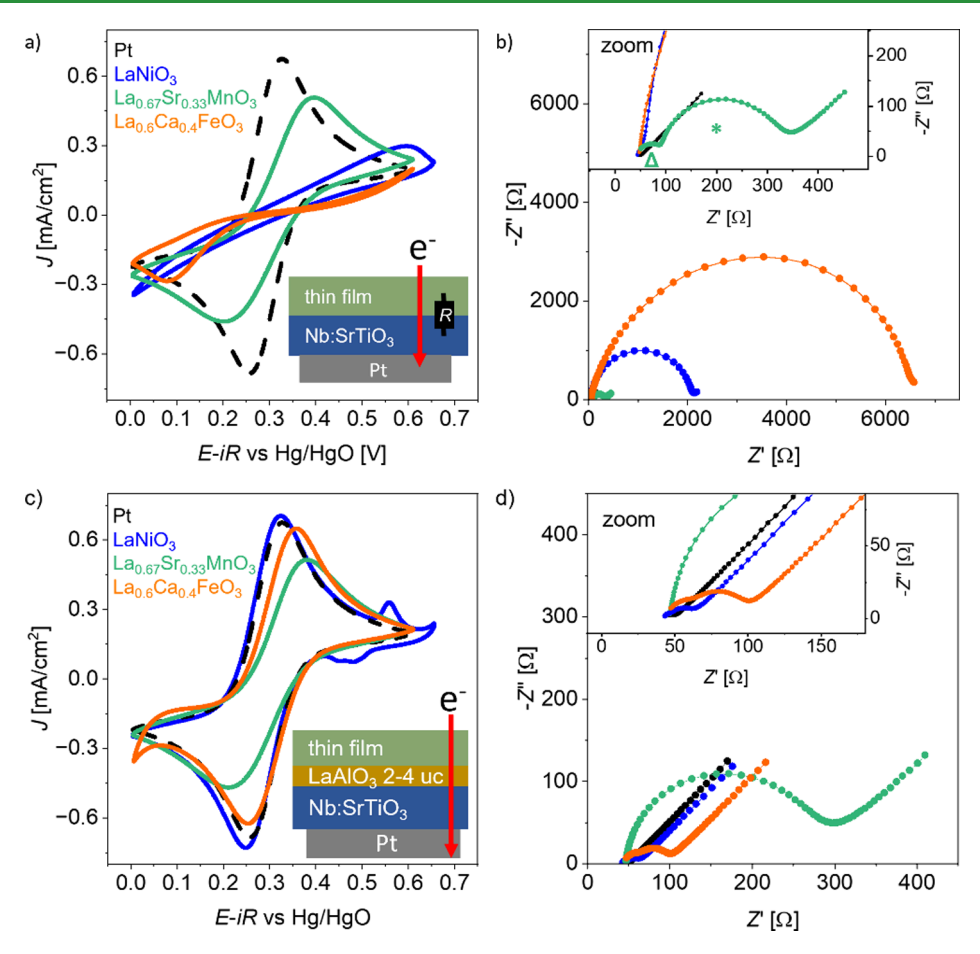


Figure 3. (a) CV in hexacyanoferrate(II)/(III) electrolyte for LaNiO<sub>3-δ</sub>, La<sub>0.67</sub>Sr<sub>0.33</sub>MnO<sub>3-δ</sub>, and La<sub>0.6</sub>Ca<sub>0.4</sub>FeO<sub>3-δ</sub> thin films grown on Nb:SrTiO<sub>3</sub> in comparison to the platinum sample. The sweep rate was 30 mV/s. (b) Corresponding impedance spectra at the OCP. Legend corresponds to (a). Inset shows the zoom of the lower impedance values.  $\Delta$  refers to the semicircle in the high frequency range of La<sub>0.67</sub>Sr<sub>0.33</sub>MnO<sub>3-δ</sub> and \* refers to the semicircle toward lower frequencies. (c) CV in hexacyanoferrate(II)/(III) electrolyte for Nb:SrTiO<sub>3</sub>/2 uc LaAlO<sub>3</sub>/LaNiO<sub>3-δ</sub>, Nb:SrTiO<sub>3</sub>/4 uc LaAlO<sub>3</sub>/La<sub>0.67</sub>Sr<sub>0.33</sub>MnO<sub>3-δ</sub> and Nb:SrTiO<sub>3</sub>/4 uc LaAlO<sub>3</sub>/La<sub>0.66</sub>Ca<sub>0.4</sub>FeO<sub>3-δ</sub> thin films in comparison to the platinum sample. The sweep rate was 30 mV/s. For LaNiO<sub>3-δ</sub>, additional oxidation and reduction peaks are seen at 0.55 and 0.45 V vs Hg/HgO, respectively, representing the Ni<sup>2+</sup>/Ni<sup>3+</sup> redox reaction. (d) Corresponding impedance spectra at the OCP. Inset shows the zoom to the lower impedance values.

potential distribution could also occur in the catalyst bulk where not solely ohmic resistances are present but also capacitive contributions  $^{43,44}$  might be present in the lateral dimension. Hence, the catalyst bulk might also be described as 2D distributed RC elements along the lateral dimension. Therefore,  $R_{\rm u}$  determined by the x-axis intercept of the impedance at high frequencies does not include all relevant bulk-related impedances. In other words, each location on the sample surface exhibits a different 'effective'  $iR_{\rm u}$  value, resulting from increasing series resistances from the edge to the center. This might explain the fact that the linear slope observed for La<sub>0.6</sub>Ca<sub>0.4</sub>FeO<sub>3- $\delta$ </sub> in Figure 1a cannot be compensated by a classic  $iR_{\rm u}$  correction.

To suppress electron transport limitations and the large radial current density distribution of the resistive thin film electrocatalysts, the chosen OER catalyst layers were deposited on 0.5 wt % Nb-doped SrTiO<sub>3</sub> (Nb:SrTiO<sub>3</sub>), which possesses metallic conductivity in the bulk. As sketched in Figure 3a, the electrons can now travel from the solid/liquid interface directly through the only nanometers thick films into the Nb:SrTiO<sub>3</sub> substrate, which can act as a current collector. The film thickness is 10 nm for LaNiO<sub>3- $\delta$ 1</sub> 20 nm for La<sub>0.6</sub>Ca<sub>0.4</sub>FeO<sub>3- $\delta$ 1</sup> and 25 nm for La<sub>0.67</sub>Sr<sub>0.33</sub>MnO<sub>3- $\delta$ 1</sub>, which is far above the thickness where finite size phenomena occur. Here, Pt is</sub>

sputtered only on the back side of the substrate. In this contacting geometry,  $La_{0.6}Ca_{0.4}FeO_{3-\delta}$  and notably also  $LaNiO_{3-\delta}$  show largely suppressed current densities and large peak separations in the hexacyanoferrate(II)/(III) redox reaction (Figure 3a), while the current density of  $La_{0.67}Sr_{0.33}MnO_{3-\delta}$  is the closest to the Pt reference and the peak separation is much smaller. This indicates that although the traveling distance has changed from a few millimeters in lateral dimensions to a few nanometers in vertical dimension in this sample geometry, the charge transport remains limited. This is particularly observed for the OER catalyst with the lowest (La<sub>0.6</sub>Ca<sub>0.4</sub>FeO<sub>3- $\delta$ </sub>) and largest (LaNiO<sub>3- $\delta$ </sub>) conductivity, indicating a departure from the systematic scaling with electrical conductivity as observed before. Instead, the observed behavior suggests an interfacial contact resistance across the substrate/thin film interface, 45-48 resulting from Schottky-type space charge layers.

For a Schottky barrier (the catalyst work function is higher than the Nb:SrTiO<sub>3</sub> electron affinity), it is expected that the electron transport is more hampered for the oxidation reaction rather than for the reduction reaction. For La<sub>0.6</sub>Ca<sub>0.4</sub>FeO<sub>3- $\delta$ 1</sub> the oxidation and reduction peaks of hexacyanoferrate(II)/(III) are asymmetric, indicating that the (Schottky-barriertype) contact resistance at the Nb:SrTiO<sub>3</sub>/thin film interface

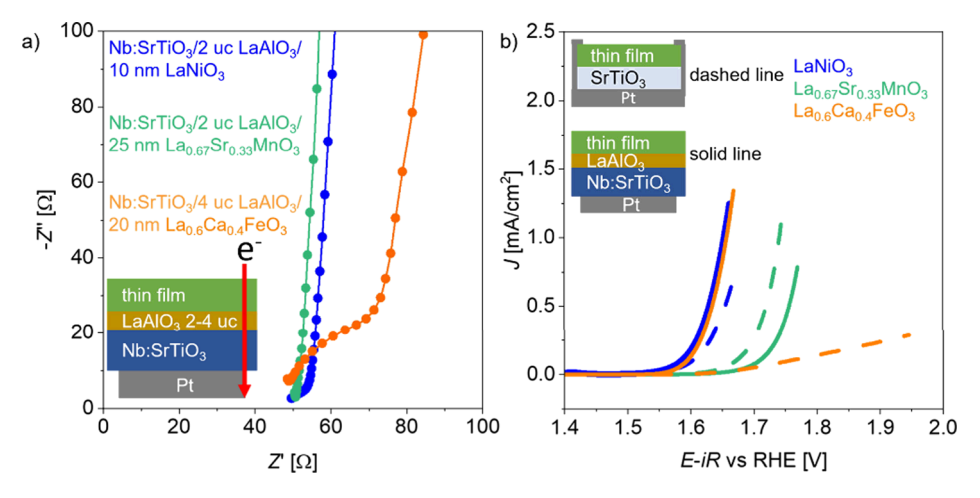


Figure 4. (a) Impedance spectra in the high frequency range at the OCP for the thin films on Nb:SrTiO<sub>3</sub> with a LaAlO<sub>3</sub> interlayer recorded in 0.1 M KOH solution. (b) OER catalytic activity of LaNiO<sub>3-δ</sub>, La<sub>0.67</sub>Sr<sub>0.33</sub>MnO<sub>3-δ</sub>, and La<sub>0.6</sub>Ca<sub>0.4</sub>FeO<sub>3-δ</sub> thin films in 0.1 M KOH for the two different contacting geometries sketched in the top left corner. OER performance of the insulating SrTiO<sub>3</sub> substrates is shown as dashed lines (reproduced from Figure 1c for ease of comparison), and the OER activities of Nb:SrTiO<sub>3</sub>/2 uc LaAlO<sub>3</sub>/LaNiO<sub>3-\delta</sub>, Nb:SrTiO<sub>3</sub>/2 uc LaAlO<sub>3</sub>/La<sub>0.67</sub>Sr<sub>0.33</sub>MnO<sub>3-\delta</sub> and Nb:SrTiO $_3$ /4 uc LaAlO $_3$ /La $_{0.6}$ Ca $_{0.4}$ FeO $_{3-\delta}$  stacks are shown as solid lines. The sweep rate was 10 mV/s.

especially hampers the oxidation from hexacyanoferrate(II) to hexacyanoferrate(III). A similar interface resistance is expected for LaNiO<sub>3-δ</sub>, which has a work function larger than the Nb:SrTiO<sub>3</sub> electron affinity, as described elsewhere. <sup>30,45,46</sup> However, the Ni oxidation takes place in the same measured potential window<sup>27</sup> as the Fe oxidation, therefore the Ni<sup>3+</sup> and Fe<sup>3+</sup> formation might lead to additional asymmetric behavior in the anodic sweep compared to the cathodic sweep seen in Figure 3a.

The Nyquist plots in Figure 3b show large semicircles for  $La_{0.6}Ca_{0.4}FeO_{3-\delta}$  and  $LaNiO_{3-\delta}$  with a real impedance (Z') of up to several  $k\Omega$ , which may be attributed to the substrate/thin film contact resistance. In contrast, La<sub>0.67</sub>Sr<sub>0.33</sub>MnO<sub>3-δ</sub> exhibits two semicircles that are below 400  $\Omega$  (marked with a green \* and  $\Delta$  in the inset of Figure 3b), indicating a significantly lower contact resistance at the substrate/thin film interface, consistent with the smaller peak separation and higher current densities in the hexacyanoferrate(II)/(III) redox reaction compared to La<sub>0.6</sub>Ca<sub>0.4</sub>FeO<sub>3-δ</sub> and LaNiO<sub>3-δ</sub>. The semicircle in the high frequency range (marked with  $\Delta$ ) of  $La_{0.67}Sr_{0.33}MnO_{3-\delta}$  could stem from the Nb:SrTiO<sub>3</sub>/thin film interface impedance, and the semicircle toward lower frequencies (\*) could stem from La<sub>0.67</sub>Sr<sub>0.33</sub>MnO<sub>3-6</sub>-specific and contact-independent behavior as the same order of magnitude impedance was already observed on the insulating substrate (Figure 2b).

The Nyquist plots in Figure 3b show that  $R_u$  is now in the same range of  $40-50 \Omega$  for all three materials, indicating that the additional ohmic resistance of the resistive La<sub>0.6</sub>Ca<sub>0.4</sub>FeO<sub>3-δ</sub> thin film that was observed in Figure 2b is circumvented in this geometry. Nevertheless, the large contact resistance to the substrate, especially for La<sub>0.6</sub>Ca<sub>0.4</sub>FeO<sub>3-δ</sub> and LaNiO<sub>3-δ</sub>, still affects the electrochemical performance and thus hinders the observation of intrinsic catalytic properties of the OER.

To decrease the contact resistance between the thin film and Nb:SrTiO<sub>3</sub>, a 2–4 uc (unit cell) thick interlayer of LaAlO<sub>3</sub> was introduced (see the sketch in Figure 3c; corresponding RHEED data are shown in Figure S7). This polar oxide layer induces an electrical dipole which can counteract interfacial space charge layers and Schottky barriers, facilitating the electron transport across the interface. <sup>21,30,49</sup> We note that the ideal dipole layer thickness to compensate for the built-in potentials is specific to the materials at the interface. For the LaNiO<sub>3 $\delta$ </sub> /Nb:SrTiO<sub>3</sub> interface, 2 unit cells (uc) of LaAlO<sub>3</sub> as interlayer effectively decreased the contact resistance, as evident by the resulting CV scan in the hexacyanoferrate-(II)/(III) redox couple (Figure 3c) and the impedance at OCP (Figure 3d), both of which are now similar to the Pt reference (Figures 3c and 3d). This shows a clear improvement in comparison to the LaNiO<sub>3-δ</sub>/Nb:SrTiO<sub>3</sub> sample without the LaAlO<sub>3</sub> interlayer (Figure 3a and 3b).

In the case of  $La_{0.67}Sr_{0.33}MnO_{3-\delta}$ , introducing 2 uc of  $LaAlO_3$ results in a slightly smaller peak separation as can be seen in the hexacyanoferrate(II)/(III) CV scan (comparing Figures 3a and 3c with 0.2 and 0.17 V peak separation, respectively) but still exhibits a small remaining overpotential. Comparing the impedance data of  $La_{0.67}Sr_{0.33}MnO_{3-\delta}$  with and without a LaAlO<sub>3</sub> interlayer on Nb:SrTiO<sub>3</sub> in Figures 3b and 3d shows that with the LaAlO<sub>3</sub> interlayer, the semicircle in the high frequency range  $(\Delta)$  is not visible anymore but the semicircle marked with a \* in Figure 3b remains. The LaAlO3 interlayer might have compensated for the smaller interface resistance at the Nb:SrTiO<sub>3</sub>/La<sub>0.67</sub>Sr<sub>0.33</sub>MnO<sub>3-δ</sub> interface, but an additional La<sub>0.67</sub>Sr<sub>0.33</sub>MnO<sub>3-6</sub>-specific impedance behavior remains, which was observed in all contacting geometries.

For La<sub>0.6</sub>Ca<sub>0.4</sub>FeO<sub>3-δ</sub>, a LaAlO<sub>3</sub> interlayer thickness of 4 uc was required to sufficiently decrease the Nb:SrTiO<sub>3</sub>/  $La_{0.6}Ca_{0.4}FeO_{3-\delta}$  contact resistance. For the Nb:SrTiO<sub>3</sub>/ LaAlO<sub>3</sub>/La<sub>0.6</sub>Ca<sub>0.4</sub>FeO<sub>3-δ</sub> stack, the reduction peak from hexacyanoferrate(III) to hexacyanoferrate(II) shows now similar behavior as the Pt sample (Figure 3c) and the oxidation peak exhibits only a small overpotential. The total impedance was reduced by 2 orders of magnitude by the 4 uc thick LaAlO<sub>3</sub> interlayer, comparing the impedance in Figure 3b and 3d. Only two small semicircles remain that are observed in the Nyquist plot in Figure 3d. The small remaining overpotential of the oxidation reaction might stem from a small remaining contact resistance at the Nb:SrTiO<sub>3</sub>/LaAlO<sub>3</sub>/ La<sub>0.6</sub>Ca<sub>0.4</sub>FeO<sub>3-δ</sub> interface and/or from an La<sub>0.6</sub>Ca<sub>0.4</sub>FeO<sub>3-δ</sub>specific resistance. As a result, the electrochemical performance in this geometry should not be strongly limited by electronic transport anymore, despite the high resistivity of

 $La_{0.6}Ca_{0.4}FeO_{3-\delta}.$  This is evidenced by the high currents obtained with the outer-sphere fast redox couple. This indicates that electronic transport limitations are also negligible for electrocatalytic inner-sphere redox reactions such as OER, implying that the measured electrocatalytic current in this geometry directly scales with the intrinsic ability of  $La_{0.6}Ca_{0.4}FeO_{3-\delta}$  to catalyze the reaction of interest, here the OER.  $^{24}$ 

Hence, the three perovskites grown on Nb:SrTiO<sub>3</sub> with LaAlO<sub>3</sub> as the charge compensating interlayer were tested in 0.1 M KOH to reveal the intrinsic catalytic activity in the OER with minimized electron transport limitations through the bulk and substrate interface resistance. Note that in contrast to the experiments in hexacyanoferrate(II)/(III) containing electrolyte, RDE rotation is set to 1600 rpm for OER experiments to remove evolving oxygen gas from the surface during the CV scan. Figure 4a shows the corresponding impedance in 0.1 M KOH of the Nb:SrTiO<sub>3</sub>/LaAlO<sub>3</sub>/catalyst stacks. The  $R_{11}$  is small  $(40-50 \Omega)$  for the three perovskite oxides, indicating no significant ohmic losses through bulk resistivities are present, which is consistent with the observation of the impedance in the hexacyanoferrate(II)/(III) containing electrolyte. For  $La_{0.6}Ca_{0.4}FeO_{3-\delta}$ , there is a small semicircle observed (~20  $\Omega$ ) in the high frequency range, which can stem from a small remaining contact resistance at the La<sub>0.6</sub>Ca<sub>0.4</sub>FeO<sub>3-δ</sub>/LaAlO<sub>3</sub>/ Nb:SrTiO<sub>3</sub> interface. The equivalent circuit and corresponding impedance fit are shown in Figure S9. Overall, however, the  $R_{\rm u}$ and the contact resistances to the substrate show significantly lower absolute values than those observed in the initial in-plane geometry and LaAlO<sub>3</sub> free thin film stacks on Nb:SrTiO<sub>3</sub>, indicating a successful removal of the OER-performance limiting current paths.

Figure 4b shows the comparison of the OER activity of the two different contacting geometries, SrTiO<sub>3</sub>/catalyst and Nb:SrTiO<sub>3</sub>/LaAlO<sub>3</sub>/catalyst. The SrTiO<sub>3</sub>/LaNiO<sub>3-δ</sub> and Nb:SrTiO<sub>3</sub>/LaAlO<sub>3</sub>/LaNiO<sub>3- $\delta$ </sub> stacks show a similar  $\eta$  of 0.37 and 0.36 V at 0.1 mA/cm<sup>2</sup>, respectively.  $La_{0.67}Sr_{0.33}MnO_{3-\delta}$ shows a higher  $\eta$  than LaNiO<sub>3- $\delta$ </sub> in both contacting geometries with  $\eta = 0.44$  and 0.48 V at 0.1 mA/cm<sup>2</sup> for the SrTiO<sub>3</sub>/  $La_{0.67}Sr_{0.33}MnO_{3-\delta}$  and Nb:SrTiO<sub>3</sub>/LaAlO<sub>3</sub>/La<sub>0.67</sub>Sr<sub>0.33</sub>MnO<sub>3-\delta</sub> stacks, respectively. The deviation between the samples can occur because of small remaining contact resistances to the Nb:SrTiO<sub>3</sub> substrate or because of sample-to-sample deviation.  $La_{0.6}Ca_{0.4}FeO_{3-\delta}$  exhibits very high  $\eta$  on the insulating substrate (0.53 V at 0.1 mA/cm<sup>2</sup>, as already introduced in Figure 1b), but the Nb:SrTiO<sub>3</sub>/LaAlO<sub>3</sub>/La<sub>0.6</sub>Ca<sub>0.4</sub>FeO<sub>3-δ</sub> stack shows a remarkably low  $\eta$  of 0.36 V at 0.1 mA/cm<sup>2</sup>, which is similar to that of LaNiO<sub>3-δ</sub>. To determine whether the CV curves shown in Figure 4b are dominated by resistances or the OER kinetics, the Tafel plots are compared in Figure S8. They show that La<sub>0.6</sub>Ca<sub>0.4</sub>FeO<sub>3-δ</sub> deposited on insulating SrTiO<sub>3</sub> strongly deviates from Tafel-like behavior, reaching values above 500 mV/dec, while on Nb:SrTiO<sub>3</sub>/LaAlO<sub>3</sub> stacks, all three perovskites show reasonable Tafel slope values between 40 mV/dec and 90 mV/dec. This highlights that in a well-chosen contacting geometry, iR correction by the x-axis intercept is reasonable and that we can reveal the intrinsic catalytic activity of poorly conducting electrocatalysts.

Hence,  $La_{0.6}Ca_{0.4}FeO_{3-\delta}$  exhibits a similar intrinsic catalytic activity in the OER as  $LaNiO_{3-\delta}$ , although it has 3 orders of magnitude higher resistivity. In turn,  $La_{0.67}Sr_{0.33}MnO_{3-\delta}$ , exhibiting intermediate resistivity among the three tested perovskites, shows the lowest intrinsic OER catalytic activity

compared to LaNiO $_{3-\delta}$  and La $_{0.6}$ Ca $_{0.4}$ FeO $_{3-\delta}$ . As a result, the intrinsic OER activity of the perovskite oxides does not scale monotonically with their electronic resistivity, and in fact, even a high resistivity perovskite can exhibit high OER performance—a result that could not have been revealed without dedicated and systematic choice of the sample substrate and interfacial layers.

#### DISCUSSION

By tuning the bulk electron transport from millimeter to nanometer scales and additionally minimizing the contact resistance in the sample stack, the intrinsic catalytic properties in the OER could be revealed for LaNiO<sub>3-δ</sub>, La<sub>0.67</sub>Sr<sub>0.33</sub>MnO<sub>3-δ</sub>, and even for the highly resistive  $La_{0.6}Ca_{0.4}FeO_{3-\delta}$ . The observed OER overpotential trend changes from  $\eta(\text{LaNiO}_{3,\delta})$  <  $\eta(\text{La}_{0.67}\text{Sr}_{0.33}\text{MnO}_{3-\delta}) < \eta(\text{La}_{0.6}\text{Ca}_{0.4}\text{FeO}_{3-\delta})$ , as observed in resistance-dominated geometry with inhomogeneous current contribution across the catalyst interface, to  $\eta(\text{LaNiO}_{3-\delta}) \approx$  $\eta(La_{0.6}Ca_{0.4}FeO_{3-\delta}) < \eta(La_{0.67}Sr_{0.33}MnO_{3-\delta})$  as the intrinsic catalytic activity trend. Hence, the intrinsic properties of perovskite catalysts do not necessarily scale with their resistivity when catalyst bulk electron transport is limited to small distances. We note that it is expected that the electronic structure, covalency, and hybridization vary among the samples. Yet, the metallic LaNiO<sub>3-δ</sub> and the highly resistive La<sub>0.6</sub>Ca<sub>0.4</sub>FeO<sub>3-δ</sub> still show remarkably similar intrinsic OER activity, provided that the current pathways are properly controlled.

However, even small residual interface resistances like the remaining interface resistance of around 20  $\Omega$  at the Nb:SrTiO $_3/\text{LaAlO}_3/\text{La}_{0.6}\text{Ca}_{0.4}\text{FeO}_{3-\delta}$  interface might affect the overall observed overpotential, diluting the revelation of intrinsic properties. This is especially noticeable at higher current densities. For small currents such as 0.1 mA, a 20  $\Omega$  series resistance leads to a 2 mV additional ohmic overpotential, whereas for 10 mA this already leads to a 200 mV ohmic overpotential. Additionally, as such Schottky-barrier-type resistances are voltage dependent, the interface resistance might change with applied potential, which might dilute the revelation of intrinsic properties as well.

A similar OER activity trend compared to our findings for the Nb:SrTiO<sub>3</sub>/LaAlO<sub>3</sub>/thin film stacks was obtained for  $LaNiO_{3-\delta},\ La_{0.75}Ca_{0.25}FeO_{3-\delta},\ La_{0.5}Ca_{0.5}FeO_{3-\delta},\ and$  $La_{0.5}Ca_{0.5}MnO_{3-\delta}$  at 50  $\mu$ A/cm<sup>2</sup> by Suntivich et al. in powder experiments (grain size  $0.2-1.0 \mu m$ ) with conductive carbon.<sup>5</sup> In their study, a lower activity was observed also for the manganite La<sub>0.5</sub>Ca<sub>0.5</sub>MnO<sub>3-δ</sub> compared to the nickelate and calcium doped ferrates ( $\eta$  (LaNiO<sub>3- $\delta$ </sub>)  $\approx \eta$  (La<sub>0.5</sub>Ca<sub>0.5</sub>FeO<sub>3- $\delta$ </sub>) <  $\eta$  (La<sub>0.5</sub>Ca<sub>0.5</sub>MnO<sub>3- $\delta$ </sub>)). In contrast, it is also reported in the literature that especially La $_{0.6}$ Ca $_{0.4}$ FeO $_{3-\delta}$  in the solid solution series of  $La_{1-x}Ca_xFeO_{3-\delta}$  has a low catalytic activity<sup>29</sup> with an overpotential (at  $50 \,\mu\text{A/cm}^2$ ) comparable to what we observed for  $La_{0.6}Ca_{0.4}FeO_{3-\delta}$  on the insulating substrate with a long bulk electron transport pathway. Also, the previously reported Tafel slope was 242 mV/dec for La<sub>0.6</sub>Ca<sub>0.4</sub>FeO<sub>3-δ</sub>, exceeding reasonable OER Tafel slope values between 30 and 120 mV/ dec by far, similar to our La<sub>0.6</sub>Ca<sub>0.4</sub>FeO<sub>3-δ</sub> sample on the insulating substrate. One reason for the higher overpotentials and Tafel slopes observed (compared to our Nb:SrTiO<sub>3</sub>/  $LaAlO_{3}/La_{0.6}Ca_{0.4}FeO_{3-\delta}$  sample and to the findings of Suntivich et al.) could be a larger grain size in the catalyst powder of the highly resistive La<sub>0.6</sub>Ca<sub>0.4</sub>FeO<sub>3-δ</sub>. This could extend the electron transport pathway through the powder

bulk significantly, even with conductive carbon, so that larger current losses occur. Additionally, conductive carbon can, for example, change the valence state of the B-site or act as a cocatalyst, 8,50,51 hindering to reveal intrinsic catalytic properties as well.

Our findings and the comparison to the literature indicate that the establishment of catalyst design rules must be taken with care, especially when materials across large resistivity ranges are tested and substrate-to-catalyst contact resistances occur. One design rule addressed in the literature stems from the observation that a small charge transfer energy leads to higher OER activity. 11 However, a large charge transfer energy (which is the energy distance between the occupied O 2p and first unoccupied transition metal 3d states) typically also leads to a lower conductivity, which can lead to lower measured (but not lower intrinsic) OER activity. 11 Therefore, it is crucial not to assume a direct correlation between low conductivity and low OER catalytic activity, which has become obvious from our revelation that metal oxides with low conductivity can exhibit a high catalytic activity. Extra steps must be taken to disentangle intrinsic catalytic activity from conductivity to accurately assess performance. As we have shown, this can be achieved by using epitaxial model systems with appropriate current collectors and favorable interface properties.

### CONCLUSION

We have shown that highly resistive perovskite oxides can be intrinsically as active as quasi metallic electrocatalysts in the OER. We decoupled the bulk resistivity and substrate/thin film contact resistances from intrinsic catalytic processes at the solid/liquid interface for the three perovskites LaNiO<sub>3-81</sub>  $La_{0.67}Sr_{0.33}MnO_{3-\delta}$ , and  $La_{0.6}Ca_{0.4}FeO_{3-\delta}$  by keeping the electron transport pathway through the catalyst bulk on the nanometer scale and minimizing the contact resistance to the Nb:SrTiO<sub>3</sub> substrate. Through the insertion of a LaAlO<sub>3</sub> dipole layer, the contact resistance between Nb:SrTiO<sub>3</sub> and catalyst was strongly decreased. Thus, we could reveal that  $LaNiO_{3-\delta}$  and  $La_{0.6}Ca_{0.4}FeO_{3-\delta}$  have similar intrinsic catalytic properties, even though La<sub>0.6</sub>Ca<sub>0.4</sub>FeO<sub>3-δ</sub> has 3 orders of magnitude higher resistivity compared to LaNiO38.  $La_{0.67}Sr_{0.33}MnO_{3-\delta}$  has intrinsically a lower OER activity compared to those of  $La_{0.6}Ca_{0.4}FeO_{3-\delta}$  and  $LaNiO_{3-\delta}$ . Hence, electrical conductivity does not necessarily correlate with intrinsic catalytic properties. Therefore, it is of high importance to quantify electron pathway dependent current density losses in chosen sample geometries as well as to distinguish intrinsic properties from resistivity for the establishment of OER catalyst design rules.

# **■ EXPERIMENTAL METHODS**

Thin Film Fabrication. The epitaxial thin films were deposited by PLD on single crystal SrTiO $_3$  and Nb:SrTiO $_3$  10 × 10 mm² substrates in the (100) orientation. LaNiO $_{3-\delta}$  was grown with a fluence of 1.9 J/cm² with a pulse repetition rate of 2 Hz, with a target-to-substrate distance of 50 mm and with an oxygen partial pressure of 0.04 mbar at 450 °C (650 °C respectively for the sample discussed in Figures 2a and 2b; the growth temperature can have an influence on the catalytic activity but does not drastically change the conductivity that is important for the hexacyanoferrate(II)/(III) CV experiment²7). La $_{0.67}$ Sr $_{0.33}$ MnO $_{3-\delta}$  was grown with a fluence of 2 J/cm², with a pulse repetition rate of 2 Hz and target-to-substrate distance of 50 mm at a growth temperature of 750 °C and an oxygen partial pressure of 0.266 mbar. The LaAlO $_3$  interlayer between Nb:SrTiO $_3$  and LaNiO $_{3-\delta}$  and La $_{0.67}$ Sr $_{0.33}$ MnO $_{3-\delta}$ , respectively, was grown with a

fluence of 1.4 J/cm², 1 Hz pulse repetition rate at a growth temperature of 650 °C, and an oxygen partial pressure of 0.002 mbar. La<sub>0.6</sub>Ca<sub>0.4</sub>FeO<sub>3- $\delta$ </sub> was deposited at 650 °C, with a laser fluence of 2.2 J/cm² and an oxygen partial pressure of 0.05 mbar, and the target-to-substrate distance was 55 mm. An LaAlO<sub>3</sub> interlayer was grown on Nb:SrTiO<sub>3</sub> at 700 °C with 1.8 J/cm² laser fluence and 1 × 10<sup>-4</sup> mbar oxygen partial pressure.

**Physical Characterization.** AFM scans were recorded with a Cypher SPM (Research Asylum, Germany) atomic force microscope in tapping mode. XRD was conducted with a D8 ADVANCE diffractometer (Bruker AXS GmbH, Germany) that was equipped with a Cu cathode for  $K_{\alpha}$  radiation, and the scans were recorded in  $2\theta$ - $\omega$  geometry.

Electrochemical Characterization. To ensure electrical contact in the electrochemical cell, the samples deposited on SrTiO3 were sputtered with 50 nm Pt on the back side, edges, and front edges (as shown in Figure S2). Samples grown on Nb:SrTiO3 were sputtered only from the back side. Electrochemical measurements of the thin films were conducted with a RDE with a rotation speed of 1600 rpm in a three-electrode configuration in 0.1 M KOH. The KOH pellets were provided from Sigma-Aldrich (purity 99.99%) and dissolved in deionized water (Milli-Q, >18.2 M $\Omega$ ·cm). The counter electrode was a spiraled Pt wire. The reference electrode was a Hg/HgO electrode protected from the solution by a Teflon tube filled with 1 M KOH. The thin films were mounted on the RDE with a custom-made PEEK holder. The thin film back side and front edges were sealed with an Oring from the electrolyte. Here, the back of the substrate is mechanically pressed against the rotary shaft of the RDE. The geometric surface area that is exposed to the electrolyte is equal to the inner area of the O-ring.

To obtain the OER activity in 0.1 M KOH, the electrolyte was purged with an O<sub>2</sub> gas for 30 min before and during the measurement. Before the determination of the OER activity with CV, impedance spectroscopy was recorded at the OCP and double layer capacitance measurements were conducted in the range from 0.0 to 0.1 V vs Hg/ HgO (for  $La_{0.6}Ca_{0.4}FeO_{3-\delta}$  from 0.1 to 0.2 V) with an increasing scan rate from 10 to 500 mV/s. To record the redox behavior of LaNiO<sub>3-δ</sub> thin films, the potential window from 0.2 to 0.65 V vs Hg/HgO was recorded with an increasing scan rate from 10 to 500 mV/s. To determine the OER activity, CV scans were conducted from 0.2 to 1.15 V vs Hg/HgO to reach at least 0.5 mA/cm<sup>2</sup>. OER currents were normalized by the geometric surface area, as appropriate for epitaxial thin films<sup>25</sup> and as justified by the low measured specific surface area. While powder catalyst activity is typically determined above 10 mA/ cm<sup>2</sup>, epitaxial thin film activity determination is appropriate at a current density of 0.1 mA/cm<sup>2</sup> as they exhibit such smooth and single-crystal-like surface morphologies.<sup>25</sup> Hence, the OER performance was determined in a current range not exceeding 1.2 mA/cm<sup>2</sup>. The Hg/HgO electrode was calibrated against the RHE (HydroFlex, USA). The averaged value of 0.887 V vs Hg/HgO was used to determine the obtained voltage on the RHE scale. The impedance was recorded in a frequency range of 100 kHz to 0.1 Hz with an amplitude of 20 mV. As the uncompensated resistance is observed in the range of 10 kHz, the spectra are shown for data points from 10 kHz and below (see for clarity Figure S4). Electrochemical measurements with the hexacyanoferrate(II)/(III) redox couple were conducted in a 0.1 M KOH solution with an equimolar concentration of 0.003 mol/L of K<sub>4</sub>[Fe(CN)<sub>6</sub>] [H<sub>2</sub>O] and K<sub>3</sub>[Fe(CN)<sub>6</sub>] (Sigma-Aldrich, 99.5% and 99.0%). The RDE rotation was off for the experiments in the  $\label{eq:hexacyanoferrate} \dot{\text{(II)}/\text{(III)}} \ \ \text{containing} \ \ \text{electrolyte.} \ \ \text{Impedance} \ \ \text{was}$ recorded at the OCP and CV scans were recorded between 0 and 0.6 V vs Hg/HgO. For LaNiO<sub>3-δ</sub>, the window was extended to 0.65 V vs Hg/HgO to obtain a possible contribution from Ni oxidation.

COMSOL Study. Simulations for the current density distribution along the film/electrolyte interface were carried out in COMSOL Multiphysics 6.2 by using the electric current (ec) module. A detailed sketch, description of the simulation, and the corresponding parameter values can be found in Figure S5. Current is injected from the Pt back electrode of the substrate and travels to the thin film edge and subsequently to the sample center with resistivities, as listed

in the main text. The electrons travel through an interfacial boundary layer to the electrolyte with a resistance that was set to 100  $\Omega$ , representing typical charge transfer resistances at low applied voltage. Finally, they travel through the electrolyte to the counter electrode (ground). As the thin film has a large aspect ratio (25 nm thickness vs 3.75 cm length, i.e., the distance from the sample center to the Oring), initial coarse simulations were carried out to optimize the geometry and mesh as much as possible. Here, we used a 2D axisymmetric geometry to further reduce the number of mesh elements. As expected, since the substrate has a very large resistance, no current flows from the Pt electrode through the substrate itself. Hence, in the final model, the substrate was removed to reduce the amount of mesh elements. A combination of free quad and boundary layer meshes was used to create a mesh with a high quality while keeping the number of meshing elements in a reasonable range (mesh sketch can be found in the Figure S5). The current densities  $J_z(x)$ shown in Figure 2c are extracted by a line cut at the boundary between the thin film and the electrolyte.

#### ASSOCIATED CONTENT

#### **Data Availability Statement**

Data are available from the authors upon reasonable request.

#### Supporting Information

The Supporting Information is available free of charge at https://pubs.acs.org/doi/10.1021/acsami.4c20141.

> RHEED, AFM, and XRD of LaNiO<sub>3-δ</sub>,  $La_{0.67}Sr_{0.33}MnO_{3\text{-}\delta}\text{, and }La_{0.6}Ca_{0.4}FeO_{3\text{-}\delta}\text{ thin films;}$ sketch of thin film placement on the RDE and sketch of O-ring placement and sputtered Pt contacts; methodology of averaging the CV forward and backward sweep; impedance spectra at high frequencies showing reference electrode contribution; COMSOL simulation sketch, parameter values, mesh, and simulation description; heat map of Figure 2d on a logarithmic scale; RHEED of 2 unit cell LaAlO<sub>3</sub> deposition and subsequent LaNiO<sub>3-δ</sub> deposition; Tafel plot and its first derivative of Figure 4b; and equivalent circuit and impedance fit of the Nb:SrTiO<sub>3</sub>/LaAlO<sub>3</sub>/La<sub>0.6</sub>Ca<sub>0.4</sub>FeO<sub>3-δ</sub> stack in Figure 4a (PDF)

#### AUTHOR INFORMATION

#### **Corresponding Authors**

Lisa Heymann - Peter Gruenberg Institute 7, Forschungszentrum Juelich GmbH, 52428 Juelich, Germany; orcid.org/0000-0002-0207-7840; Email: l.heymann@fzjuelich.de

Felix Gunkel – Peter Gruenberg Institute 7, Forschungszentrum Juelich GmbH, 52428 Juelich, Germany; Email: f.gunkel@fz-juelich.de

Christoph Baeumer - Peter Gruenberg Institute 7, Forschungszentrum Juelich GmbH, 52428 Juelich, Germany; MESA+ Institute for Nanotechnology, Faculty of Science and Technology, University of Twente, 7500 AE Enschede, Email: c.baeumer@utwente.nl

### **Authors**

Iris C. G. van den Bosch – MESA+ Institute for Nanotechnology, Faculty of Science and Technology, University of Twente, 7500 AE Enschede, Netherlands

Daan H. Wielens - MESA+ Institute for Nanotechnology, Faculty of Science and Technology, University of Twente, 7500 AE Enschede, Netherlands; o orcid.org/0000-0002-2816-9671

Ole Kurbjeweit - Peter Gruenberg Institute 7, Forschungszentrum Juelich GmbH, 52428 Juelich, Germany Emma van der Minne – MESA+ Institute for Nanotechnology, Faculty of Science and Technology, University of Twente, 7500 AE Enschede, Netherlands Ellen M. Kiens – MESA+ Institute for Nanotechnology, Faculty of Science and Technology, University of Twente, 7500 AE Enschede, Netherlands; o orcid.org/0000-0003-

Anton Kaus – Peter Gruenberg Institute 7, Forschungszentrum Juelich GmbH, 52428 Juelich, Germany Daniel Schön - Peter Gruenberg Institute 7,

Forschungszentrum Juelich GmbH, 52428 Juelich, Germany Stephan Menzel - Peter Gruenberg Institute 7,

Forschungszentrum Juelich GmbH, 52428 Juelich, Germany; orcid.org/0000-0002-4258-2673

Bernard Boukamp – MESA+ Institute for Nanotechnology, Faculty of Science and Technology, University of Twente, 7500 AE Enschede, Netherlands; oorcid.org/0000-0001-7348-5385

Complete contact information is available at: https://pubs.acs.org/10.1021/acsami.4c20141

#### **Author Contributions**

L.H., I.v.d.B., F.G., and C.B. conceived and designed the experiments. L.H. and I.v.d.B conducted electrochemical experiments. L.H., I.v.d.B., E.v.d.M., and E.K. fabricated the thin film samples. L.H. and E.v.d.M. conducted resistivity measurements. D.W. conceptualized and conducted the COMSOL simulations. D.S. and S.M. refined the mesh of the COMSOL model. O.K. and A.K. provided experimental support and scientific discussion. B.B. advised on an in-depth understanding of impedance data. L.H., I.v.d.B., B.B., F.G., and C.B. conducted in-depth scientific discussions on electrochemical and physical analysis during the whole experimental progress. L.H., I.v.d.B., D.W., F.G., and C.B. wrote the manuscript with contributions from all authors. F.G. and C.B. supervised the research project.

The authors declare no competing financial interest.

#### **ACKNOWLEDGMENTS**

We thank Grigory Potemkin, Shreyas Harsha, and Tursun Abudukade for the experimental support. We thank Dr. Marco Altomare for the insightful discussion. We gratefully acknowledge funding from the European Union (ERC, 101040669 -Interfaces at Work). Views and opinions expressed are however those of the author(s) only and do not necessarily reflect those of the European Union or the European Research Council. Neither the European Union nor the granting authority can be held responsible for them. A.K. and F.G. acknowledge funding by the German Research Foundation in the framework of the SPP 2080, project no 493705276 (GU1604/4).

## REFERENCES

- (1) International Energy Agency. Future of Hydrogen; International Energy Agency (IEA), 2019. https://www.iea.org/reports/the-futureof-hydrogen.
- (2) Carrara, S.; Bobba, S.; Blagoeva, D.; Alves Dias, P.; Cavalli, A.; Georgitzikis, K.; Grohol, K.; Itul, A.; Kuzov, T.; Latunussa, C.; Lyons, L.; Malano, G.; Maury, T.; Prior Arce, A.; Somers, J.; Telsnig, T.; Veeh, C.; Wittmer, D.; Black, C.; Pennington, D.; Christou, M. Supply Chain Analysis and Material Demand Forecast in Strategic Technologies

- and Sectors in the EU A Foresight Study; Policy Assessment, Anticipation and Foresight, Risk Assessment KJ-NA-31-437-EN-N (online), KJ-NA-31-437-EN-C (print); Publications Office of the European Union: Luxembourg (Luxembourg), 2023. DOI: 10.2760/386650 (online), DOI: 10.2760/334074 (print).
- (3) Xie, X.; Du, L.; Yan, L.; Park, S.; Qiu, Y.; Sokolowski, J.; Wang, W.; Shao, Y. Oxygen Evolution Reaction in Alkaline Environment: Material Challenges and Solutions. *Adv. Funct. Mater.* **2022**, 32 (21), No. 2110036.
- (4) Liu, J.; Liu, H.; Chen, H.; Du, X.; Zhang, B.; Hong, Z.; Sun, S.; Wang, W. Progress and Challenges Toward the Rational Design of Oxygen Electrocatalysts Based on a Descriptor Approach. *Advanced Science* **2020**, *7* (1), No. 1901614.
- (5) Suntivich, J.; May, K. J.; Gasteiger, H. A.; Goodenough, J. B.; Shao-Horn, Y. A Perovskite Oxide Optimized for Oxygen Evolution Catalysis from Molecular Orbital Principles. *Science* **2011**, 334 (6061), 1383–1385.
- (6) Gunkel, F.; Christensen, D. V.; Chen, Y. Z.; Pryds, N. Oxygen Vacancies: The (in)Visible Friend of Oxide Electronics. *Appl. Phys. Lett.* **2020**, *116* (12), No. 120505.
- (7) George, G.; Ede, S. R.; Luo, Z. Fundamentals of Perovskite Oxides: Synthesis, Structure, Properties and Applications, 1st ed.; CRC Press, 2020.
- (8) Liu, L.-B.; Yi, C.; Mi, H.-C.; Zhang, S. L.; Fu, X.-Z.; Luo, J.-L.; Liu, S. Perovskite Oxides Toward Oxygen Evolution Reaction: Intellectual Design Strategies, Properties and Perspectives. *Electrochemical Energy Reviews* **2024**, *7* (1), 14.
- (9) Lakhanlal; Caspary Toroker, M. Filling the Gaps on the Relation between Electronic Conductivity and Catalysis of Electrocatalysts for Water Splitting Using Computational Modelling. *Current Opinion in Electrochemistry* **2023**, *40*, No. 101342.
- (10) Cheng, X.; Fabbri, E.; Yamashita, Y.; Castelli, I. E.; Kim, B.; Uchida, M.; Haumont, R.; Puente-Orench, I.; Schmidt, T. J. Oxygen Evolution Reaction on Perovskites: A Multieffect Descriptor Study Combining Experimental and Theoretical Methods. *ACS Catal.* **2018**, 8 (10), 9567–9578.
- (11) Hong, W. T.; Stoerzinger, K. A.; Lee, Y.-L.; Giordano, L.; Grimaud, A.; Johnson, A. M.; Hwang, J.; Crumlin, E. J.; Yang, W.; Shao-Horn, Y. Charge-Transfer-Energy-Dependent Oxygen Evolution Reaction Mechanisms for Perovskite Oxides. *Energy Environ. Sci.* 2017, 10 (10), 2190–2200.
- (12) Egelund, S.; Caspersen, M.; Nikiforov, A.; Møller, P. Manufacturing of a LaNiO<sub>3</sub> Composite Electrode for Oxygen Evolution in Commercial Alkaline Water Electrolysis. *Int. J. Hydrogen Energy* **2016**, *41* (24), 10152–10160.
- (13) Zou, S.; Burke, M. S.; Kast, M. G.; Fan, J.; Danilovic, N.; Boettcher, S. W. Fe (Oxy)Hydroxide Oxygen Evolution Reaction Electrocatalysis: Intrinsic Activity and the Roles of Electrical Conductivity, Substrate, and Dissolution. *Chem. Mater.* **2015**, 27 (23), 8011–8020.
- (14) Burke, M. S.; Enman, L. J.; Batchellor, A. S.; Zou, S.; Boettcher, S. W. Oxygen Evolution Reaction Electrocatalysis on Transition Metal Oxides and (Oxy)Hydroxides: Activity Trends and Design Principles. *Chem. Mater.* **2015**, 27 (22), 7549–7558.
- (15) Fan, L.; Rautama, E. L.; Lindén, J.; Sainio, J.; Jiang, H.; Sorsa, O.; Han, N.; Flox, C.; Zhao, Y.; Li, Y.; Kallio, T. Two Orders of Magnitude Enhancement in Oxygen Evolution Reactivity of  $La_{0.7}Sr_{0.3}Fe_{1-x}Ni_xO_{3-\delta}$  by Improving the Electrical Conductivity. *Nano Energy* **2022**, *93*, No. 106794.
- (16) Stoerzinger, K. A.; Choi, W. S.; Jeen, H.; Lee, H. N.; Shao-Horn, Y. Role of Strain and Conductivity in Oxygen Electrocatalysis on LaCoO<sub>3</sub> Thin Films. *J. Phys. Chem. Lett.* **2015**, *6* (3), 487–492.
- (17) Yun, T. G.; Heo, Y.; Bin Bae, H.; Chung, S.-Y. Elucidating Intrinsic Contribution of D-Orbital States to Oxygen Evolution Electrocatalysis in Oxides. *Nat. Commun.* **2021**, *12* (1), 824.
- (18) Heymann, L.; Weber, M. L.; Wohlgemuth, M.; Risch, M.; Dittmann, R.; Baeumer, C.; Gunkel, F. Separating the Effects of Band Bending and Covalency in Hybrid Perovskite Oxide Electrocatalyst

- Bilayers for Water Electrolysis. ACS Appl. Mater. Interfaces 2022, 14 (12), 14129–14136.
- (19) Akbashev, A. R.; Zhang, L.; Mefford, J. T.; Park, J.; Butz, B.; Luftman, H.; Chueh, W. C.; Vojvodic, A. Activation of Ultrathin SrTiO<sub>3</sub> with Subsurface SrRuO<sub>3</sub> for the Oxygen Evolution Reaction. *Energy Environ. Sci.* **2018**, *11* (7), 1762–1769.
- (20) Baniecki, J. D.; Yamaguchi, H.; Harnagea, C.; Ricinschi, D.; Gu, Z.; Spanier, J. E.; Yamazaki, T.; Aso, H. Enhanced Stability and Thickness-Independent Oxygen Evolution Electrocatalysis of Heterostructured Anodes with Buried Epitaxial Bilayers. *Adv. Energy Mater.* **2019**, 9 (28), No. 1803846.
- (21) Yajima, T.; Hikita, Y.; Minohara, M.; Bell, C.; Mundy, J. A.; Kourkoutis, L. F.; Muller, D. A.; Kumigashira, H.; Oshima, M.; Hwang, H. Y. Controlling Band Alignments by Artificial Interface Dipoles at Perovskite Heterointerfaces. *Nat. Commun.* **2015**, *6* (1), 6759.
- (22) Burton, A. R.; Paudel, R.; Matthews, B.; Sassi, M.; Spurgeon, S. R.; Farnum, B. H.; Comes, R. B. Thickness Dependent OER Electrocatalysis of Epitaxial LaFeO $_3$  Thin Films. *J. Mater. Chem. A* **2022**, *10* (4), 1909–1918.
- (23) Weber, M. L.; Gunkel, F. Epitaxial Catalysts for Oxygen Evolution Reaction: Model Systems and Beyond. *Journal of Physics: Energy* **2019**, *1* (3), No. 031001.
- (24) Antipin, D.; Risch, M. Trends of Epitaxial Perovskite Oxide Films Catalyzing the Oxygen Evolution Reaction in Alkaline Media. *Journal of Physics: Energy* **2020**, 2 (3), No. 032003.
- (25) Adiga, P.; Stoerzinger, K. A. Epitaxial Oxide Thin Films for Oxygen Electrocatalysis: A Tutorial Review. *Journal of Vacuum Science* & *Technology A* **2022**, 40 (1), No. 010801.
- (26) Füngerlings, A.; Wohlgemuth, M.; Antipin, D.; van der Minne, E.; Kiens, E. M.; Villalobos, J.; Risch, M.; Gunkel, F.; Pentcheva, R.; Baeumer, C. Crystal-Facet-Dependent Surface Transformation Dictates the Oxygen Evolution Reaction Activity in Lanthanum Nickelate. *Nat. Commun.* 2023, 14 (1), 8284.
- (27) Baeumer, C.; Li, J.; Lu, Q.; Liang, A. Y.-L.; Jin, L.; Martins, H. P.; Duchoň, T.; Glöß, M.; Gericke, S. M.; Wohlgemuth, M. A.; Giesen, M.; Penn, E. E.; Dittmann, R.; Gunkel, F.; Waser, R.; Bajdich, M.; Nemšák, S.; Mefford, J. T.; Chueh, W. C. Tuning Electrochemically Driven Surface Transformation in Atomically Flat LaNiO<sub>3</sub> Thin Films for Enhanced Water Electrolysis. *Nat. Mater.* **2021**, *20* (5), 674–682.
- (28) Stoerzinger, K. A.; Risch, M.; Suntivich, J.; Lu, W. M.; Zhou, J.; Biegalski, M. D.; Christen, H. M.; Ariando; Venkatesan, T.; Shao-Horn, Y. Oxygen Electrocatalysis on (001)-Oriented Manganese Perovskite Films: Mn Valency and Charge Transfer at the Nanoscale. *Energy Environ. Sci.* **2013**, *6*, 1582.
- (29) Sankannavar, R.; Sarkar, A. The Electrocatalysis of Oxygen Evolution Reaction on  $La_{1-x}Ca_xFeO_{3-\delta}$  Perovskites in Alkaline Solution. *Int. J. Hydrogen Energy* **2018**, 43 (9), 4682–4690.
- (30) Nishio, K.; Shirasawa, T.; Shimizu, K.; Nakamura, N.; Watanabe, S.; Shimizu, R.; Hitosugi, T. Tuning the Schottky Barrier Height at the Interfaces of Metals and Mixed Conductors. *ACS Appl. Mater. Interfaces* **2021**, *13* (13), 15746–15754.
- (31) Sergeenkov, S.; Cichetto, L.; Zampieri, M.; Longo, E.; Araújo-Moreira, F. M. Scaling like Behaviour of Resistivity Observed in LaNiO<sub>3</sub> Thin Films Grown on SrTiO<sub>3</sub> Substrate by Pulsed Laser Deposition. *J. Phys.: Condens. Matter* **2015**, 27 (48), No. 485307.
- (32) Yin, H. Q.; Zhou, J.-S.; Goodenough, J. B. Near-Room-Temperature Tunneling Magnetoresistance in a Trilayer La<sub>0.67</sub>Sr<sub>0.33</sub>MnO<sub>3</sub>/La<sub>0.85</sub>Sr<sub>0.15</sub>MnO<sub>3</sub>/La<sub>0.67</sub>Sr<sub>0.33</sub>MnO<sub>3</sub> Device. *Appl. Phys. Lett.* **2000**, *77* (5), 714–716.
- (33) Boschker, H; Huijben, M; Vailionis, A; Verbeeck, J; van Aert, S; Luysberg, M; Bals, S; van Tendeloo, G; Houwman, E P; Koster, G; Blank, D H A; Rijnders, G Optimized Fabrication of High-Quality La<sub>0.67</sub>Sr<sub>0.33</sub>MnO<sub>3</sub> Thin Films Considering All Essential Characteristics. *J. Phys. D: Appl. Phys.* **2011**, 44 (20), No. 205001.
- (34) Irmak, A. E. Structural and Electrical Properties of Ca<sup>2+</sup> Doped LaFeO<sub>3</sub>: The Effect of A-Site Cation Size Mismatch. *Engineering, Technology & Applied Science Research* **2020**, 10 (2), 5538–5546.

- (35) Tran, A.-T.; Huet, F.; Ngo, K.; Rousseau, P. Artefacts in Electrochemical Impedance Measurement in Electrolytic Solutions Due to the Reference Electrode. *Electrochim. Acta* **2011**, *56* (23), 8034–8039.
- (36) Davies, T. J.; Banks, C. E.; Compton, R. G. Voltammetry at Spatially Heterogeneous Electrodes. *J. Solid State Electrochem.* **2005**, 9 (12), 797–808.
- (37) Muralidharan, V. B. Warburg Impedance Basics Revisited. *Anti-Corrosion Methods and Materials* **1997**, 44 (1), 26–29.
- (38) Newman, J. Currents below the Limiting Current. In Electrochemical Systems; John Wiley & Sons, 2021.
- (39) Hirschorn, B.; Orazem, M. E.; Tribollet, B.; Vivier, V.; Frateur, I.; Musiani, M. Determination of Effective Capacitance and Film Thickness from Constant-Phase-Element Parameters. *Electrochim. Acta* **2010**, *55* (21), *6218–6227*.
- (40) Huang, V. M.-W.; Vivier, V.; Orazem, M. E.; Pébère, N.; Tribollet, B. The Apparent Constant-Phase-Element Behavior of a Disk Electrode with Faradaic Reactions: A Global and Local Impedance Analysis. *J. Electrochem. Soc.* **2007**, *154* (2), C99.
- (41) Pospisil, J.; Marackova, L.; Zmeskal, O.; Kovalenko, A. Universal Approach for Diffusion Quantification Applied to Lead Halide Perovskite Single Crystals. *Appl. Phys. A: Mater. Sci. Process.* **2023**, *129* (2), *129*.
- (42) Oldham, K. B. Edge Effects in Semiinfinite Diffusion. *Journal of Electroanalytical Chemistry and Interfacial Electrochemistry* **1981**, 122, 1–17.
- (43) Balaya, P.; Jamnik, J.; Fleig, J.; Maier, J. Mesoscopic Hole Conduction in Nanocrystalline SrTiO3: A Detailed Analysis by Impedance Spectroscopy. *J. Electrochem. Soc.* **2007**, *154* (6), P69.
- (44) Menke, T.; Meuffels, P.; Dittmann, R.; Szot, K.; Waser, R. Separation of Bulk and Interface Contributions to Electroforming and Resistive Switching Behavior of Epitaxial Fe-Doped SrTiO3. *J. Appl. Phys.* **2009**, *105* (6), No. 066104.
- (45) Chien, T.; Liu, J.; Yost, A. J.; Chakhalian, J.; Freeland, J. W.; Guisinger, N. P. Built-in Electric Field Induced Mechanical Property Change at the Lanthanum Nickelate/Nb-Doped Strontium Titanate Interfaces. Sci. Rep. 2016, 6 (1), No. 19017.
- (46) Yoo, H. K.; Chang, Y. J.; Moreschini, L.; Kim, H.-D.; Sohn, C. H.; Sinn, S.; Oh, J. S.; Kuo, C.-T.; Bostwick, A.; Rotenberg, E.; Noh, T. W. Insulating-Layer Formation of Metallic LaNiO<sub>3</sub> on Nb-Doped SrTiO<sub>3</sub> Substrate. *Appl. Phys. Lett.* **2015**, *106* (12), No. 121601.
- (47) Lu, H. X.; Zhang, J.; Zhang, H. R.; Li, Y.; Chen, Y. S.; Shen, B. G.; Sun, J. R. A Conductive Scanning Study of  $La_{0.67}Sr_{0.33}MnO_3/Nb:SrTiO_3$  Hetero-Junction. *Appl. Phys. Lett.* **2016**, *108* (5), No. 051608.
- (48) Zhan, J. M.; Li, P. G.; Liu, H.; Tao, S. L.; Ma, H.; Shen, J. Q.; Pan, M. J.; Zhang, Z. J.; Wang, S. L.; Yuan, G. L. Carrier Tuning the Metal-Insulator Transition of Epitaxial La<sub>0.67</sub>Sr<sub>0.33</sub>MnO<sub>3</sub> Thin Film on Nb Doped SrTiO<sub>3</sub> Substrate. *AIP Advances* **2016**, *6* (4), No. 045001.
- (49) Hikita, Y.; Nishio, K.; Seitz, L. C.; Chakthranont, P.; Tachikawa, T.; Jaramillo, T. F.; Hwang, H. Y. Band Edge Engineering of Oxide Photoanodes for Photoelectrochemical Water Splitting: Integration of Subsurface Dipoles with Atomic-Scale Control. *Adv. Energy Mater.* **2016**, *6* (7), No. 1502154.
- (50) Mohamed, R.; Cheng, X.; Fabbri, E.; Levecque, P.; Kötz, R.; Conrad, O.; Schmidt, T. J. Electrocatalysis of Perovskites: The Influence of Carbon on the Oxygen Evolution Activity. *J. Electrochem. Soc.* **2015**, *162* (6), F579.
- (51) Zhu, Y.; Zhou, W.; Shao, Z. Perovskite/Carbon Composites: Applications in Oxygen Electrocatalysis. *Small* **2017**, *13* (12), No. 1603793.